Rectangular photonic crystal nanobeam cavities in bulk diamond

Rectangular photonic crystal nanobeam cavities in bulk diamond

Sara Mouradian, Noel H. Wan, Tim Schröder, and Dirk Englund

Citation: Appl. Phys. Lett. **111**, 021103 (2017);
View online: https://doi.org/10.1063/1.4992118
View Table of Contents: http://aip.scitation.org/toc/apl/111/2
Published by the American Institute of Physics

Rectangular photonic crystal nanobeam cavities in bulk diamond

Sara Mouradian,[1,a)] Noel H. Wan,[1,a)] Tim Schröder,[1,2] and Dirk Englund[1,b)]
[1]*Department of Electrical Engineering and Computer Science, Massachusetts Institute of Technology, Cambridge Massachusetts 02139, USA*
[2]*Niels Bohr Institute, University of Copenhagen, 2100 Copenhagen, Denmark*

(Received 24 April 2017; accepted 24 June 2017; published online 10 July 2017)

We demonstrate the fabrication of photonic crystal nanobeam cavities with rectangular cross section into bulk diamond. In simulation, these cavities have an unloaded quality (Q) factor of over 1×10^6. Measured cavity resonances show fundamental modes with spectrometer-limited Q factors $\geq 14 \times 10^3$ within 1 nm of the nitrogen vacancy centers zero phonon line at 637 nm. We find high cavity yield across the full diamond chip with deterministic resonance trends across the fabricated parameter sweeps. *Published by AIP Publishing.* [http://dx.doi.org/10.1063/1.4992118]

A central aim of quantum information science is the efficient generation of large entangled states of stationary quantum memories. Among solid-state qubits, a leading system consists of the nitrogen vacancy (NV) center in diamond. Recently, entanglement between distant NV nodes has been demonstrated via single-photon measurements of the zero phonon line (ZPL) emission.[1,2] Such heralded entanglement can be used to build large cluster states[3] or quantum repeaters in a large quantum communication network.[4,5] However, the coherent ZPL optical transition of the NV accounts for only 3% of the emission due to phonon interactions. This severely limits the entanglement rate, even with broadband collection enhancement structures such as a solid immersion lens.[2] To improve the entanglement rate, the collection rate into the desired frequency and spatial mode must be increased. Much recent work has focused on maximizing the coherent ZPL collection efficiency via the Purcell effect.[6–21]

One major challenge in coupling the NV to a nanocavity is that high-quality diamond membranes of the thickness ($\sim$200 nm) required for nanocavities cannot currently be grown. Hybrid structures have been used to enhance the ZPL emission,[7,22,23] though the maximum enhancement rate is limited as the NV must be placed out of the cavity's mode maximum. Advances in diamond patterning have enabled the fabrication of photonic crystal cavities in diamond[24] with two main methods: fabrication into membranes thinned from bulk diamond[10–17] and angled etching of bulk diamond to form suspended structures.[18–21] However, the measured quality (Q) factors have been limited to a few thousand near the NV ZPL. Low cavity yield across the diamond substrate also presents a major scaling challenge, especially for membrane-based approaches due to thickness variations in the starting membranes.[24–26]

Recently, Khanaliloo *et al.*[27,28] introduced a technique to undercut lithographically defined structures in bulk diamond, similar to techniques used to fabricate freestanding MEMS structures in bulk Si.[29] In this letter, we apply a similar isotropic undercut process to the fabrication of photonic crystal nanobeam cavities from bulk diamond. Figure 1(a) shows a schematic of the rectangular nanobeam photonic crystal cavity fabricated in bulk diamond. We find that the quasi-isotropic etching procedure is highly repeatable, and that the process requires minimal fabrication optimization as electron-beam lithography determines all parameters except for the nanobeam height, which can be precisely tuned during the relatively slow isotropic etching. This fabrication process enables instrument-limited optical quality (Q) factors exceeding 14 000 within 1 nm of the NV^- center ZPL wavelength of 637 nm, as well as uniform nanocavity fabrication across a full chip.

We design photonic crystal nanobeam cavities to support a mode with low mode volume (V), high Q factor at the NV ZPL (637 nm), and with the electric-field maximum concentrated in the diamond. The design process begins with approximate cavity parameters derived from band structure simulations and optimizes the cavity Q of the lowest order TE mode [intensity profile shown in Fig. 1(b)] at $\lambda_{NV} = 637$ nm by Finite-Difference Time-Domain (FDTD) simulations. The final design consists of a diamond waveguide ($W = 250$ nm and $H = 230$ nm) periodically patterned with holes of radius $r = 58$ nm and spacing $a = 192$ nm. The defect supporting the cavity mode is introduced by linearly decreasing the hole spacing to $a = 171$ nm over 5 periods. With 25 holes on either side of the cavity region, this cavity has a radiation-limited Q factor of $>1 \times 10^6$. The simulated mode volume is $\sim(\lambda/n)^3$

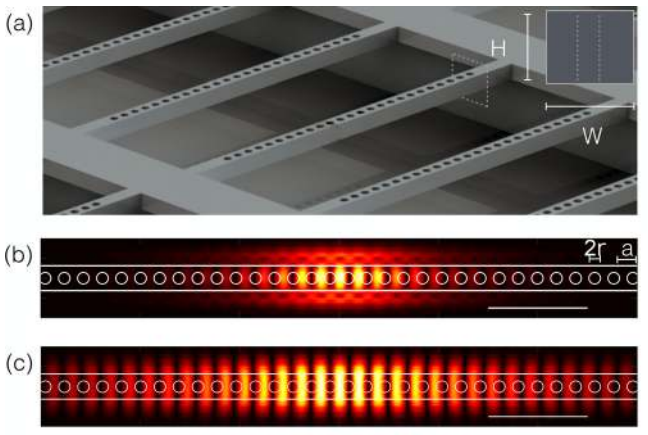

FIG. 1. (a) Schematic of an array of rectangular nanobeam cavities fabricated from bulk diamond. (b) Re($|E|^2$) for the first order TE mode. (c) Re($|E|^2$) for the first order TM mode. Scale bar for (b) and (c): 1 μm.

[a)]S. Mouradian and N. H. Wan contributed equally to this work.
[b)]englund@mit.edu.

and the Purcell factor for an optimally positioned and oriented dipole is ≥75000. The cavity also supports a TM mode [Fig. 1(c) shows the intensity profile] at 615 nm with a Q of 13 000 in simulation, as well as other TE modes with mode maxima in the outer hole regions with lower Q values—5500 and 2500 in simulation at 649 nm and 653 nm respectively. These two modes are denoted as M3 and M4 in the measured spectra in Figs. 3 and 4.

We fabricated these nanobeam cavity designs in a 3 mm × 3 mm × 0.3 mm single-crystal diamond with a {100} top face grown by chemical vapor deposition (CVD, Element6) with a nitrogen defect density of less than 1 ppm, and thus a native NV density of approximately 1 ppb. The etch rate of the quasi-isotropic etch step is facet dependent, ensuring that structures aligned with the fastest etching facet (110) will have a rectangular cross section.[28] High resolution X-ray diffraction is used to measure the crystal orientation in order to align the nanobeams correctly. Unlike nanobeam cavities with triangular cross sections which mix the TE and TM modes, these cavities have low out-of-plane scattering loss.[18,20]

Figures 2(a)–2(f) outline the essential steps of the fabrication process. A 180 nm-thick low-stress SiN layer, deposited with plasma-enhanced chemical vapor deposition, functions as a hard mask to pattern the diamond. Electron-beam lithography defines the nanobeam cavities (ZEP 520A exposed at 500 μC/cm^2 and developed at 0 °C in ortho-xylene for 90 s). Following resist development, a tetrafluoromethane (CF_4) plasma reactive-ion etch step transfers the pattern into the SiN hard mask (200 W RF, 10 Pa, ∼70 nm/min etch rate). This pattern is transferred into the diamond [Fig. 2(a)] using an inductively coupled oxygen plasma (ICP) with a working pressure of 0.15 Pa with ICP and RF powers of 500 W and 240 W, respectively. The SiN mask provides a selectivity of 30:1 for these etching parameters. This anisotropic etch step is 2.5 times as deep as the final desired cavity height so that the nanobeam height can be precisely tuned in the subsequent isotropic undercut etch step. This step produces smooth and straight sidewalls as seen in the scanning electron micrograph (SEM) in Fig. 2(g).

A conformal layer of 20 nm of aluminum oxide (Al_2O_3) produced by atomic layer deposition (ALD) [Fig. 2(b)], protects all sides of the nanobeam cavity for the subsequent etch steps. The same CF_4 reactive ion etch used for the SiN etching removes the top Al_2O_3 layer (∼10 nm/min), leaving only the sides covered [Fig. 2(c)]. A second anisotropic oxygen etch, using the same parameters as above, removes an additional 1 μm of diamond [Fig. 2(d)]. A quasi-isotropic oxygen etch then undercuts the nanobeam structure at 200 °C and 3 Pa with 900 W ICP and no forward bias [Fig. 2(e)]. The elevated temperature and pressure increase the chemical interaction rate with the diamond to increase the etch rate. As seen in the SEM in Fig. 2(h), the Al_2O_3 is thin enough to allow periodic SEM measurements of the nanobeam height. Once the desired nanobeam height of 230 nm (∼85 min with an initial beam height of 575 nm) is achieved, the residual SiN and Al_2O_3 are removed using 49% hydrofluoric acid [Fig. 2(f)]. An SEM of the final structure after mask removal is shown in Fig. 2(i). Figures 2(j) and 2(k) shows a cavity broken off the bulk and laid on its side for comparison of the topside (j) and underside (k) of the cavity. This SEM confirms the rectangular cross section.

The measured chip contains 125 cavities, with 5 copies at each of 25 parameters. The parameter sweep modified the beam widths and hole radii by ±4% and ±16%, respectively, to cover a large wavelength range.

We measured the fabricated cavities at 4 K by photoluminescence (PL) and photoluminescence excitation (PLE) spectroscopy. The native population of NV centers, excited using 250 μW of 532 nm laser, provides an internal light source for the cavity. The cavity PL is collected with a 0.9 NA objective and resolved on a spectrometer with a resolution of 0.06 nm ($Q \sim 14\ 000$). Figure 3 shows two cavity spectra: Cavity A ($W = 260$ nm, $r = 55$ nm) and cavity B ($W = 245$ nm, $r = 58$ nm). Figure 3(a) shows the cavity-modified PL spectrum of the NV ensemble at cavity A under 532 nm excitation. Four modes appear in the spectrum with resonant wavelengths and Q factors corresponding to the first-order TE mode, first-order TM mode, M3, and M4. Figure 3(b) shows the high-Q first-order TE mode at 636.1 nm, as well as the inhomogeneously broadened ZPL of the excited ensemble of NV centers at 637 nm. The linewidth of the cavity mode is limited by the spectrometer's resolution, as confirmed by comparing to the

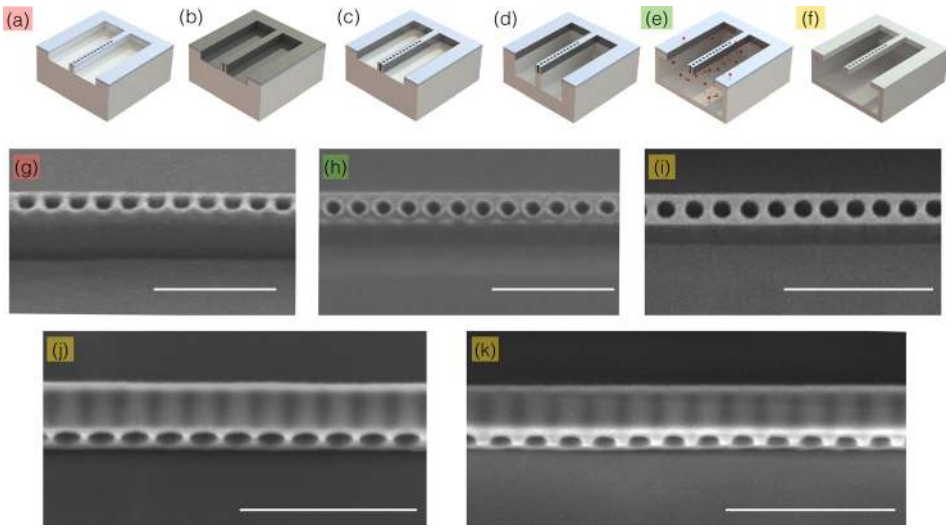

FIG. 2. (a)–(f) Fabrication steps for rectangular nanobeam photonic crystal cavities, where white, blue, and gray indicate bulk diamond, SiN, and Al_2O_3, respectively. (a) Anisotropic etch into diamond with SiN hard mask following electron-beam lithography. (b) Atomic layer deposition of Al_2O_3. (c) Selective removal of the top layer of Al_2O_3. (d) Anisotropic etch into diamond (e) Quasi-isotropic etch of diamond nanobeam cavity. (f) Suspended nanobeam cavity following mask removal. Scanning electron micrographs (SEMs) (g)–(i) correspond to processes (a), (e), and (f), respectively. (j) SEM of the top of a cavity broken off the array and placed on its side. (k) SEM of the bottom of the same cavity in (j). Scale bar on all SEM images measures 1 μm.

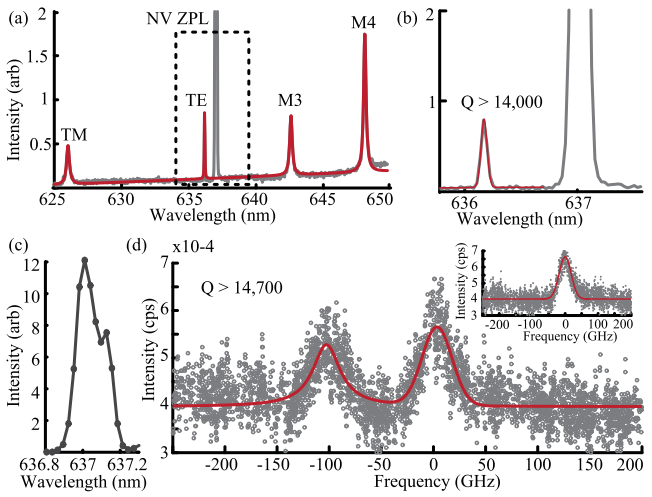

FIG. 3. (a) PL spectrum of cavity A with lowest order TE and TM cavity peaks fit with Lorentzian functions. (b) Zoom in of the fundamental TE mode of cavity A. The red line shows a fit to the spectrometer-limited cavity peak, fit with a pseudo-Voigt function. (c) PL spectrum of cavity B showing the inhomogeneously broadened ZPL emission from the ensemble of excited NVs at 637 nm and a cavity peak at 637.1 nm. (d) Photoluminescence excitation (PLE) spectrum of cavity B showing a PLE peak at NV ZPL position and a cavity-enhanced PLE peak 100 GHz detuned from the inhomogeneous ZPL distribution. The inset shows a PLE measurement of the same nanobeam 7 μm from the cavity center showing only the inhomogeneous distribution of NV centers in the sample.

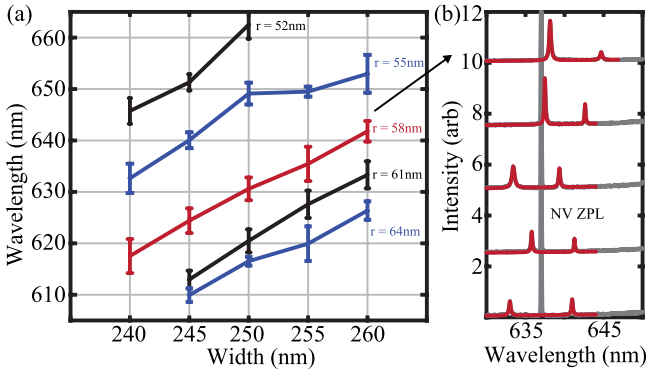

FIG. 4. (a) Frequency distribution of resonant frequencies of mode 4 for all 25 sets of parameters. The error bars show the standard deviation $\pm\sigma$ of the resonant frequencies for the 5 cavities fabricated for each set of parameters. (b) The spectra of the 5 cavities fabricated with W = 260 nm and r = 58 nm [circled in (a)] showing the distribution of mode 3 and mode 4.

spectrum of a sub-0.5 MHz laser at the same wavelength. Fitting the spectrum with a pseudo-Voigt function[30] takes into account the convolution of the Gaussian spectrometer lineshape with the Lorentzian cavity spectrum. This fit indicates a lower bound of $Q \geq 16\,700$, above the resolution of the spectrometer ($Q \geq 14\,000$).

The spectrum of cavity B [Fig. 3(c)] reveals the first-order TE mode overlapping with the inhomogeneous distribution of ZPLs in the NV ensemble. We performed PLE spectroscopy to better measure the Q of this cavity and study the cavity-enhanced excitation of the NV ensemble. The PLE consisted of NV phonon side band (PSB) detection (filtered >650 nm) while scanning a <0.5 MHz-linewidth laser (2 μW) over the NV ZPL and cavity frequencies (~637 nm). The inset of Fig. 3(d) shows the PLE spectrum of the same nanobeam 7 μm from the cavity center in a region without holes. This reveals an inhomogeneously broadened absorption spectrum of the excited population of NV centers centered at 470.48 THz (637.2 nm) with a full width half maximum of 42.7 GHz. A PLE scan at the center of the cavity shows a second peak that is absent on the rest of the sample. We attribute this to the cavity-enhanced laser absorption of NV centers coupled to the cavity mode. A Lorentzian fit of the peak reveals a measured cavity Q of 14 700. This provides a lower bound on the Q of the bare cavity mode, as the PLE spectrum may be broadened by the interaction with the inhomogeneous distribution of emitters coupled to this mode of the cavity.[31]

A survey of all of the fabricated devices demonstrates the consistency and high yield of our fabrication technique. Figure 4(a) shows the measured cavity resonances of mode M4 across the full range of parameters. The error bars show the standard deviation of the wavelength position for the 5 cavities fabricated with each parameter set. We used here mode M4 as it has the highest vertical loss of the four modes considered and thus the highest signal to noise ratio in spectrometer measurements. This survey reveals the expected trends: the resonance wavelengths increase with larger beam widths and decrease with larger holes radii. The standard deviation within each parameter is low with an average of ± 2.2 nm deviation from the mean in each parameter set, showing the consistency of the fabrication process. The spectra of M3 and M4 of the 5 cavities with $W = 260$ nm and $r = 58$ nm [circled in Fig. 4(a) are shown in Fig. 4(b)]. The small deviations in resonant wavelengths for each set of parameters most likely derives from small deviations in the shape and size of the holes due to local variations in electron beam dose and development, as well as variations in the beam dimensions.

In summary, we have demonstrated a method to fabricate high-Q photonic crystal nanobeam cavities from bulk diamond. We measured cavity resonances within 1 nm of the NV ZPL wavelength, with instrument-limited Q factors larger than 14 000. The process showed consistent cavity properties across all fabricated devices. Future work will apply this fabrication process to high-purity diamond with a nitrogen concentration below 5 ppb, which should enable the coupling of individual NV ZPLs with high Purcell enhancement. The rectangular cross section of these cavities should enable efficient mode conversion between diamond waveguides and on-chip ridge or channel waveguides for integration into a large photonic integrated circuit.[32] This fabrication technique applies to other diamond color centers, such as the germanium vacancy and silicon vacancy centers. These emitters can have naturally narrow emission linewidth[33–35] so that the nanocavity parameters achieved here should allow for the demonstration of the strong coupling regime of cavity quantum electrodynamics.

S.M. was supported in part by the NSF IQuISE program and the NSF program ACQUIRE: "Scalable Quantum Communications with Error-Corrected Semiconductor Qubits." N.W. was supported by the Army Research Laboratory Center for Distributed Quantum Information (CDQI). Fabrication was

supported in part by the STC Center for Integrated Quantum Materials (CIQM), NSF Grant No. DMR-1231319. We thank Jim Daley, Mark Mondol, and Tim Savas at the Nanostructures Laboratory at MIT for invaluable discussions and support during the development of this fabrication technique.

[1]E. Togan, Y. Chu, A. Trifonov, L. Jiang, J. Maze, L. Childress, M. G. Dutt, A. S. Sørensen, P. Hemmer, A. Zibrov *et al.*, Nature **466**, 730 (2010).
[2]H. Bernien, B. Hensen, W. Pfaff, G. Koolstra, M. S. Blok, L. Robledo, T. H. Taminiau, M. Markham, D. J. Twitchen, L. Childress, and R. Hanson, Nature **497**, 86 (2013).
[3]S. D. Barrett and P. Kok, Phys. Rev. A **71**, 060310 (2005).
[4]L. Childress, J. Taylor, A. S. Sørensen, and M. D. Lukin, Phys. Rev. A **72**, 052330 (2005).
[5]S. E. Vinay and P. Kok, Phys. Rev. A **95**, 052336 (2017).
[6]D. Riedel, I. Söllner, B. J. Shields, S. Starosielec, P. Appel, E. Neu, P. Maletinsky, and R. J. Warburton, preprint arXiv:1703.00815 (2017).
[7]M. Gould, E. R. Schmidgall, S. Dadgostar, F. Hatami, and K.-M. C. Fu, Phys. Rev. Appl. **6**, 011001 (2016).
[8]S. Bogdanović, S. B. van Dam, C. Bonato, L. C. Coenen, A.-M. J. Zwerver, B. Hensen, M. S. Liddy, T. Fink, A. Reiserer, M. Lončar *et al.*, Appl. Phys. Lett. **110**, 171103 (2017).
[9]E. Janitz, M. Ruf, M. Dimock, A. Bourassa, J. Sankey, and L. Childress, Phys. Rev. A **92**, 043844 (2015).
[10]A. Faraon, P. E. Barclay, C. Santori, K.-M. C. Fu, and R. G. Beausoleil, Nat. Photonics **5**, 301 (2011).
[11]A. Faraon, C. Santori, Z. Huang, V. M. Acosta, and R. G. Beausoleil, Phys. Rev. Lett. **109**, 033604 (2012).
[12]B. Hausmann, B. Shields, Q. Quan, Y. Chu, N. De Leon, R. Evans, M. Burek, A. Zibrov, M. Markham, D. Twitchen *et al.*, Nano Lett. **13**, 5791 (2013).
[13]J. C. Lee, D. O. Bracher, S. Cui, K. Ohno, C. A. McLellan, X. Zhang, P. Andrich, B. Alemán, K. J. Russell, A. P. Magyar *et al.*, Appl. Phys. Lett. **105**, 261101 (2014).
[14]L. Li, T. Schröder, E. H. Chen, M. Walsh, I. Bayn, J. Goldstein, O. Gaathon, M. E. Trusheim, M. Lu, J. Mower *et al.*, Nat. Commun. **6**, 6173 (2015).
[15]J. Riedrich-Möller, C. Arend, C. Pauly, F. Mücklich, M. Fischer, S. Gsell, M. Schreck, and C. Becher, Nano Lett. **14**, 5281 (2014).
[16]J. Riedrich-Möller, L. Kipfstuhl, C. Hepp, E. Neu, C. Pauly, F. Mücklich, A. Baur, M. Wandt, S. Wolff, M. Fischer, S. Gsell, M. Schreck, and C. Becher, Nat. Nanotechnol. **7**, 69 (2012).
[17]L. Li, I. Bayn, M. Lu, C.-Y. Nam, T. Schröder, A. Stein, N. C. Harris, and D. Englund, Sci. Rep. **5**, 7802 (2015).
[18]I. Bayn, B. Meyler, J. Salzman, and R. Kalish, New J. Phys. **13**, 025018 (2011).
[19]I. Bayn, S. Mouradian, L. Li, J. A. Goldstein, T. Schröder, J. Zheng, E. H. Chen, O. Gaathon, M. Lu, A. Stein, C. A. Ruggiero, J. Salzman, R. Kalish, and D. Englund, Appl. Phys. Lett. **105**, 211101 (2014).
[20]M. J. Burek, Y. Chu, M. S. Liddy, P. Patel, J. Rochman, S. Meesala, W. Hong, Q. Quan, M. D. Lukin, and M. Lončar, Nat. Commun. **5**, 5718 (2014).
[21]M. Schukraft, J. Zheng, T. Schröder, S. Mouradian, M. Walsh, M. Trusheim, H. Bakhru, and D. Englund, APL Photonics **1**, 020801 (2016).
[22]D. Englund, B. Shields, K. Rivoire, F. Hatami, J. Vuckovic, H. Park, and M. D. Lukin, Nano Lett. **10**, 3922 (2010).
[23]J. Wolters, A. W. Schell, G. Kewes, N. Nüsse, M. Schoengen, H. Döscher, T. Hannappel, B. Löchel, M. Barth, and O. Benson, Appl. Phys. Lett. **97**, 141108 (2010).
[24]T. Schröder, S. L. Mouradian, J. Zheng, M. E. Trusheim, M. Walsh, E. H. Chen, L. Li, I. Bayn, and D. Englund, J. Opt. Soc. Am. B **33**, B65 (2016).
[25]A. H. Piracha, P. Rath, K. Ganesan, S. Kuhn, W. H. Pernice, and S. Prawer, Nano Lett. **16**, 3341 (2016).
[26]P. Appel, E. Neu, M. Ganzhorn, A. Barfuss, M. Batzer, M. Gratz, A. Tschöpe, and P. Maletinsky, Rev. Sci. Instrum. **87**, 063703 (2016).
[27]B. Khanaliloo, M. Mitchell, A. C. Hryciw, and P. E. Barclay, Nano Lett. **15**, 5131 (2015).
[28]B. Khanaliloo, H. Jayakumar, A. C. Hryciw, D. P. Lake, H. Kaviani, and P. E. Barclay, Phys. Rev. X **5**, 041051 (2015).
[29]K. A. Shaw, Z. L. Zhang, and N. C. MacDonald, Sens. Actuators, A **40**, 63 (1994).
[30]R. Albrecht, A. Bommer, C. Deutsch, J. Reichel, and C. Becher, Phys. Rev. Lett. **110**, 243602 (2013).
[31]D. Valente, J. Suffczyński, T. Jakubczyk, A. Dousse, A. Lemaître, I. Sagnes, L. Lanco, P. Voisin, A. Auffèves, and P. Senellart, Phys. Rev. B **89**, 041302 (2014).
[32]S. L. Mouradian, T. Schröder, C. B. Poitras, L. Li, J. Goldstein, E. H. Chen, M. Walsh, J. Cardenas, M. L. Markham, D. J. Twitchen *et al.*, Phys. Rev. X **5**, 031009 (2015).
[33]T. Schröder, M. E. Trusheim, M. Walsh, L. Li, J. Zheng, M. Schukraft, J. L. Pacheco, R. M. Camacho, E. S. Bielejec, A. Sipahigil *et al.*, Nat. Commun. **8**, 15376 (2017).
[34]A. Sipahigil, K. D. Jahnke, L. J. Rogers, T. Teraji, J. Isoya, A. S. Zibrov, F. Jelezko, and M. D. Lukin, Phys. Rev. Lett. **113**, 113602 (2014).
[35]M. K. Bhaskar, D. D. Sukachev, A. Sipahigil, R. E. Evans, M. J. Burek, C. T. Nguyen, L. J. Rogers, P. Siyushev, M. H. Metsch, H. Park *et al.*, Phys. Rev. Lett. **118**, 223603 (2017).